A&A 472, 785–796 (2007)
DOI: 10.1051/0004-6361:20077461

Astronomy & Astrophysics

High-resolution radio continuum survey of M 33[*]

I. The radio maps

F. S. Tabatabaei[**], M. Krause, and R. Beck

Max-Planck Institut für Radioastronomie, Auf dem Hügel 69, 53121 Bonn, Germany
e-mail: `tabataba@mpifr-bonn.mpg.de`

Received 12 March 2007 / Accepted 25 May 2007

ABSTRACT

Aims. We study the exponential scale length of total radio emission, the spectral index distribution, and the linear radio polarization in the Scd galaxy M 33.

Methods. Observations were carried out using the 3.6 cm dual channel and the 6.2 cm four-channel receivers of the 100-m Effelsberg telescope along with the *L*-band VLA D-array at 20 cm.

Results. High spatial resolution and sensitivity in both total and linearly polarized radio continuum emission from M 33 were achieved. We found considerable extended emission, not only from the main arms I S and I N, but also from the weaker arms. The large-scale magnetic field exhibits well-ordered spiral structure with almost the same orientation as that of the optical spiral arms; however, it does not show a clear structural correlation or anti-correlation with the optical arms. There is a north-south asymmetry in polarization that is frequency-dependent. We found that the ring mean spectral index versus radius increases faster beyond $R = 4$ kpc. At each wavelength, the exponential scale length is larger inside than outside $R = 4$ kpc.

Conclusions. From the larger scale lengths at $R < 4$ kpc, we conclude that star-forming regions are mainly spread over the region $R <$ 4 kpc without a dominant nuclear concentration. Furthermore, at $R < 4$ kpc, a spatial correlation between cosmic rays and star-forming regions may exist. From the behavior of the mean spectral indices obtained from different pairs of the radio continuum data at 3.6, 6.2, and 20 cm, we confirm that a decrease in the thermal fraction causes an increase in the spectral index. The frequency-dependent asymmetry in the polarization hints at asymmetry in Faraday depolarization.

Key words. galaxies: individual: M 33 – radio continuum: galaxies – galaxies: magnetic fields – galaxies: ISM

1. Introduction

The nearest Scd galaxy at a distance of 840 kpc ($1'' \simeq 4$ pc, Freedman et al. 1991), M 33 (NGC 598) has been extensively studied at radio wavelengths. Terzian & Pankonin (1972) detected some diffuse emission at 318 and 606 MHz using angular resolutions of $17'$ and $10'$, respectively. Israel & van der Kruit (1974) observed M 33 at 1415 MHz with the Synthesis telescope in Westerbork (WSRT). However, they did not find any extended spiral arm emission. This emission was first revealed by observations with the 100-m Effelsberg dish at 6.2 cm (von Kap-Herr et al. 1978) that was extensively studied by Berkhuijsen (1983). Radio polarization observations of M 33 were first made by Beck (1979) at 21.1 cm and 11.1 cm. Buczilowski & Beck (1987) observed this galaxy at 17.4 cm, 6.3 cm, and 2.8 cm. They detected polarization mostly in the northern half of M 33 and proposed a bisymmetric magnetic field structure. The next interferometer observations (Duric et al. 1993; Viallefond et al. 1986; Gordon et al. 1999) were carried out in total intensity to study point sources like HII regions and supernova remnants (SNRs) within M 33.

Generally, single-dish observations should be carried out to study the extended radio emission. So far, single-dish observations have been limited by sensitivity because M 33 is relatively weak in radio emission, especially in polarized emission (with an integrated flux density of ~83 mJy at 6.2 cm, Buczilowski & Beck 1991), and because of M 33's large extent in the sky (~$35' \times 40'$).

This paper is the first in a series providing a detailed investigation of the radio continuum emission of M 33. We describe new observations of the radio continuum emission at 3.6 cm, 6.2 cm, and 20 cm with much improved detection limits of total and polarized intensity and with higher spatial resolutions. These data allow a much more detailed study of polarization and the magnetic field within M 33 than was possible before. We discuss the distribution and degree of linear polarization, integrated flux densities and distribution of the total spectral index (obtained from total intensities of the radio continuum emission including both thermal and nonthermal emission). We also compare the radial, exponential scale lengths of the radio emission at different wavelengths.

A comprehensive treatment of the separation of thermal and nonthermal emission, rotation measures, Faraday effects, depolarization, magnetic field strength and structure, radio-IR correlation, and cosmic ray distribution will be given in further papers of this series.

The observations and data reduction are described in Sect. 2. Results, including distributions of total intensity and polarization, integrated flux densities, and total spectral index

---

[*] FITS files for Fig. 1 are only available in electronic form at the CDS via anonymous ftp to `cdsarc.u-strasbg.fr (130.79.128.5)` or via
`http://cdsweb.u-strasbg.fr/cgi-bin/qcat?J/A+A/472/785`

[**] Member of the International Max Planck Research School (IMPRS) for Radio and Infrared Astronomy at the Universities of Bonn and Cologne.

Table 1. Positional data on M 33.

Nucleus position (J2000)[1]	RA = $1^{h}33^{m}51.0^{s}$ Dec = 30°39′37.0″
Position angle of major axis[2]	23°
Inclination[3]	56°
Distance[4] (1″ = 4 kpc)	840 kpc

[1] de Vaucouleurs & Leach (1981). [2] Deul & van der Hulst (1987). [3] Regan & Vogel (1994). [4] Freedman et al. (1991).

distribution, are discussed in Sect. 3. Discussion and concluding remarks are presented in Sect. 4.

2. Observations and data reduction

We performed both single-dish and interferometer observations. The single-dish observations at 3.6 cm and 6.2 cm were made with the 100-m Effelsberg telescope[1]. The interferometer observations at 20 cm were carried out with the Very Large Array (VLA[2]).

2.1. Effelsberg single-dish observations

We observed M 33 at 3.6 cm during several periods from August 2005 to March 2006 with the broadband system (bandwidth ~1100 MHz) centered at 8350 MHz. The receiver is a dual-channel correlation radiometer with cooled HEMT amplifiers and a cooled polarization transducer located in the secondary focus of the 100-m telescope. The system is set up for receiving left hand circular (LHC) and right hand circular (RLC) polarization. M 33 was scanned along RA and Dec with a scanning velocity of 50′/min on a grid of 30″. The scanned area of 40′ × 50′ was centered on the nucleus of the galaxy. The total observing time was about 100 h. We obtained 56 coverages with a typical sensitivity per scan of 2 mJy/beam area in total intensity and 0.4 mJy/beam area in polarization. The half power beam width (*HPBW*) at 3.6 cm is 83.6″ which corresponds to a linear resolution of about 335 pc.

The sources 3C 48, 3C 286, and 3C 138 were used for pointing and focusing during the observations. Calibration of the flux density and polarization angle was achieved by observing 3C 286. We used the flux density scale given by Baars et al. (1977).

The data reduction was performed in the NOD2 data reduction system (Haslam 1974). In order to remove the scanning effects due to ground radiation, weather condition, and receiver instabilities, we applied the scanning removal program, *Presse*, of Sofue & Reich (1979). The rms noise after combination of the coverages (Emerson & Graeve 1988) is ~220 μJy/beam in Stokes I (total intensity) map and ~70 μJy/beam in Stokes U and Q (polarization) maps. The final maps in U and Q were combined to produce maps in polarized intensity and in polarization angle, correcting for the positive bias in polarized intensity due to noise (Killeen et al. 1986). Figures 1 and 2 show the resulting maps of the total and polarized intensities, respectively, smoothed to an angular resolution of 120″.

Observations at 6.2 cm were carried out in the summer of 1996 using the 4850 MHz HEMT receiver installed in the secondary focus of the 100-m Effelsberg telescope. This is a 4-channel, 2-beam system with cooled HEMT pre-amplifiers (see Table 2 for more information about this receiver). M 33 was scanned along its major axis and perpendicular to it on a grid of 1′ with a scanning velocity of 90′/min. The field size is 100′ × 80′. The number of useful coverages is 12 for Stokes I maps and 14 for each of the U and Q maps. The 6.2 cm data reduction was performed similar to that at 3.6 cm. The rms noise after combination is ~700 μJy/beam in Stokes I (total intensity) map and ~180 μJy/beam in Stokes U and Q (polarization) maps. The final maps of total and polarized intensities (smoothed to 180″) are shown in Figs. 5 and 6, respectively.

2.2. VLA observations

We observed M 33 at 20 cm (L-band) in two 50 MHz bands centered at 1385 and 1465 MHz with dual circular polarization in the continuum mode of the VLA D-array. The observation dates were 06-11-05, 07-11-05, 08-11-05, 13-11-05, and 06-01-06. To cover the central 30′ × 45′ with equal sensitivity, we made a mosaic with 12 pointings with a spacing of half the primary beam width, 15′, (3 pointings along RA and 4 pointings along Dec). The coordinates of the 12 pointings are listed in Table 2. The observations were made in cycles with 6 min on each pointing of the mosaic. This observing cycle was repeated 17 times. At the beginning and end of each 4-cycle, we observed 3C 138 and 3C 48 as the primary flux density calibrators. The antenna gains and phases were calibrated every 43 min with the phase calibrator 0029 + 349. The source 3C 138 was also used for polarization calibration.

The standard procedures of the Astronomical Image Processing System (AIPS) were used to reduce the data. The data from each day were calibrated separately to ensure that there were no day-to day amplitude discrepancies. Then they were split into 12 single-source visibility data sets corresponding to the different pointings. After flagging, we combined the source visibility data from different days of the same source. We self-calibrated the combined visibility data in both phase and amplitude and phase. Final images were made with IMAGR parameter Robust = 0. The rms noise of different pointings in both total intensity (I) and polarization (U and Q) are listed in Table 3. We convolved all the single images to the largest clean beam of 51.4″ in both RA and Dec, the individual images were reprojected on a single grid centered at RA = $01^{h}33^{m}51.41^{s}$ and Dec = +30°46′45.00″. Then, we combined the single images to a mosaic with equal weights using the task "LTESS", which also corrects for primary beam attenuation.

There is a considerable lack of flux density in the VLA maps: the integrated total flux is only ~15% in total intensity and ~55% in polarized intensity of those in the Effelsberg maps (determined as described in Sect. 3.3). This is not surprising because of the missing short spacings in the forms of severe attenuation of angular scales larger than ~13′ (corresponding to the shortest spacing of ~40 m) and the negative bowl artifact around strong sources. To correct for the missing spacing, we combined the VLA map with the Effelsberg single-dish 20 cm map (Fletcher 2001) in the uv plane. To avoid distortions in the combined total intensity (I) map due to strong sources, we first subtracted these sources from the VLA map. The sources were identified in the Effelsberg map by comparing with the VLA map smoothed to the Effelsberg resolution. Then they were also subtracted from the Effelsberg map. The residual VLA and

---

[1] The 100-m telescope at Effelsberg is operated by the Max-Planck-Institut für Radioastronomie (MPIfR) on behalf on the Max-Planck-Gesellschaft.

[2] The VLA is a facility of the National Radio Astronomy Observatory. The NRAO is operated by Associated Universities, Inc., under contract with the National Science Foundation.

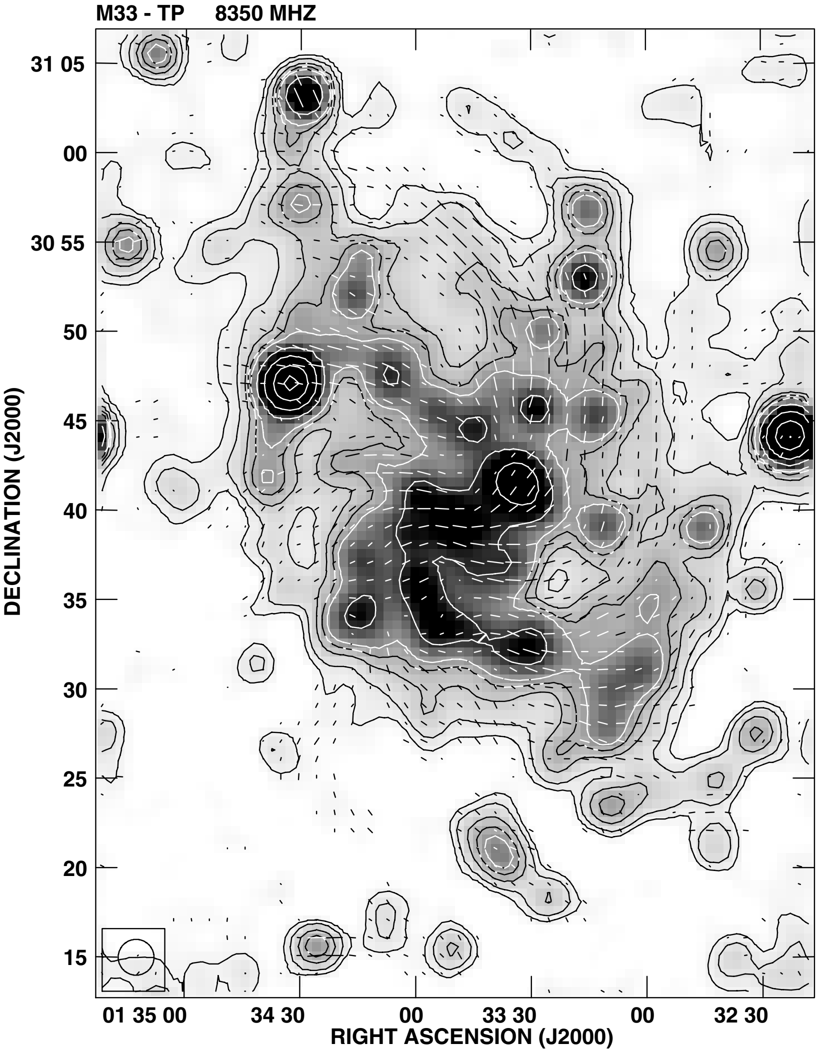

Fig. 1. Total intensity emission from M 33 at 3.6 cm observed with the Effelsberg telescope, with apparent ***B***-vectors (***E***-vectors rotated by 90°) of polarized intensity superimposed. The *HPBW* is 120″ (the beam area is shown in the left-hand corner). Contour levels are 0.5, 1, 2, 3, 4, 8, 16, 32, 64 mJy/beam. The rms noise is 0.14 mJy/beam in total intensity and 0.04 mJy/beam in linear polarization. The vectors were plotted starting from 0.1 mJy/beam (2.5σ). A vector length of 1′ represents a polarized intensity of 0.5 mJy/beam. The FITS data of the 3.6 cm total intensity is available at the CDS.

Effelsberg maps were combined using the task "IMERG" with a maximum spacing of $0.236\,\mathrm{k}\lambda$ for the Effelsberg map and a minimum spacing of $0.170\,\mathrm{k}\lambda$ for the VLA map in total intensity. The corresponding maximum and minimum spacing adopted in polarizarion (U and Q) are $0.171\,\mathrm{k}\lambda$ and $0.150\,\mathrm{k}\lambda$, respectively. These maximum and minimum spacing values were chosen so that the integrated flux densities of the merged maps became equal to those of the Effelsberg maps. After combination, the VLA point sources were added again. The rms noise in the combined maps are ~70 μJy/beam area in Stokes I and ~25 μJy/beam area in Stokes U and Q. The resulting total and polarized intensity images are shown in Figs. 7 and 8, respectively.

3. Results

3.1. Total intensity

Our total intensity map of M 33 at 3.6 cm is a factor of ~6 more sensitive than the 2.8 cm map of Buczilowski & Beck (1987). The map at 3.6 cm with the original angular resolution of 84″ was presented by Tabatabaei et al. (2007). Even after smoothing to 120″, the total intensity map (Figs. 1 and 3) shows that not only are the two main optical arms I S[3] and I N pronounced, but also the northern arms II N, III N, IV N, and V N are (at least partly) visible at 3.6 cm. The total intensity of the extended emission is about 4 mJy/beam in the arm I N which increases to 8 mJy/beam in parts of the arm I S. The intensity is lower than 3 mJy/beam in the other arms. The flux densities of 11 brightest HII regions at 3.6 cm are presented in Table 4.

At 6.2 cm, the rms noise (0.7 mJy/beam) is improved by a factor of two with respect to the previous observations by Buczilowski & Beck (1987). The northern arms and I S plus parts of the southern arms II S and III S are visible in the second contour in Fig. 5.

With a linear resolution of ~200 pc (*HPBW* = 51.4″) and a sensitivity of 70 μJy/beam, a large number of point sources are revealed in the total intensity map at 20 cm (Fig. 7). A list of the flux densities of the radio point sources at 20 cm at 7″ resolution was presented by Gordon et al. (1999)[4]. The contour levels shown in Fig. 7 starts at the 4σ level. The strongest extended emission is found in the arm I S with a flux density of ≥3.6 mJy/beam, followed by parts of the arm I N and the extended central region of the galaxy. At 20 cm, the extended emission is detected up to larger radii and is more radially symmetric than at 3.6 cm and 6.2 cm.

---

[3] We refer to the arm notation of Humphreys & Sandage (1980); I N to V N for the northern and I S to V S for the southern arms.

[4] They observed M 33 with the VLA and WSRT at 1.4 GHz and measured the flux density of point sources, but missed the extended emission.

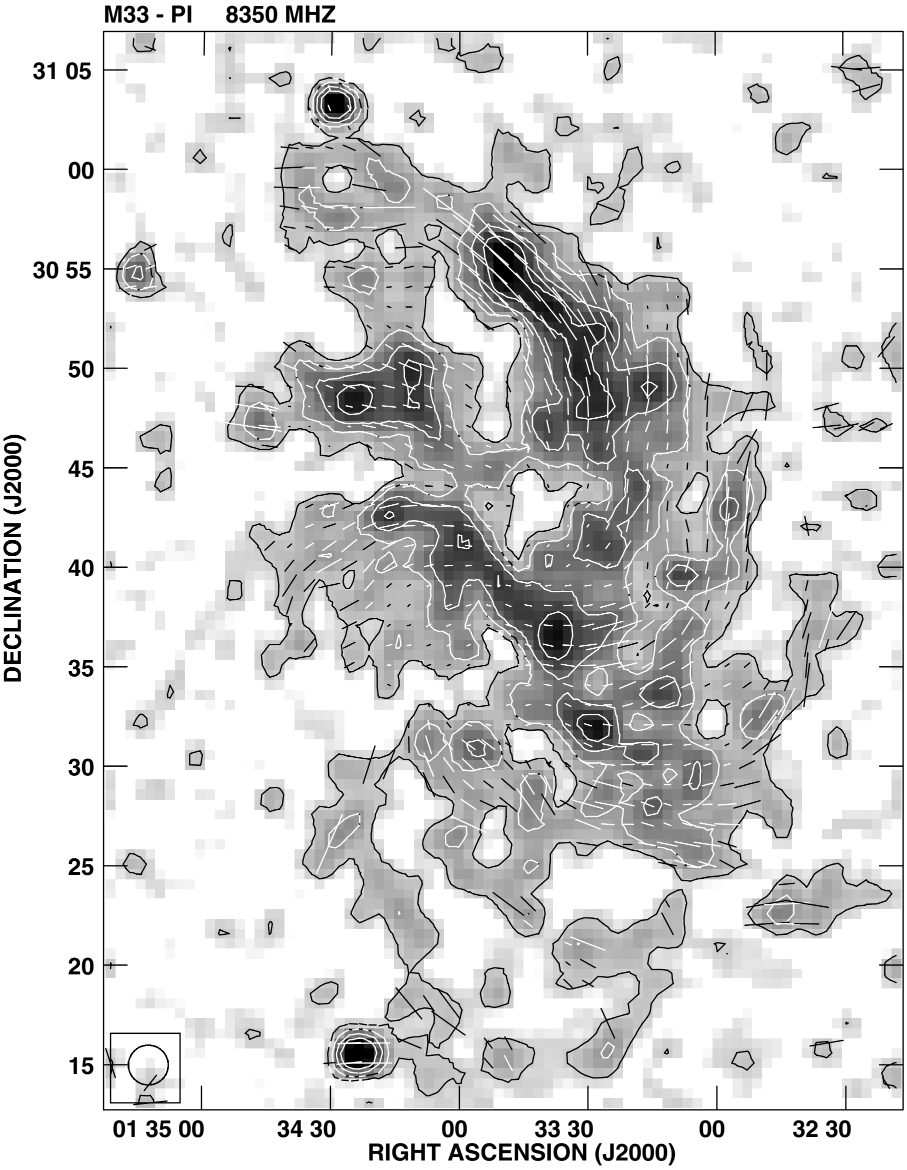

Fig. 2. Linearly polarized emission (contours and grey scale) and degree of polarization (vector lengths) from M 33 at 3.6 cm observed with the Effelsberg telescope, smoothed to an angular resolution of 120″ (the beam area is shown in the left-hand corner). Position angles of the vectors show the orientation of the apparent magnetic field component perpendicular to the line of sight. Contour levels are 0.1, 0.2, 0.3, 0.4 mJy/beam. The rms noise is 0.04 mJy/beam. A vector length of 1′ represents a degree of polarization of 12.6%.

3.2. Distribution of polarized emission

The polarized emission at 3.6 cm is shown in Fig. 2 in grey scale and with contours. A sketch of the optical spiral arms by Sandage & Humphreys (1980) superimposed on the polarized emission is shown in Fig. 3. Strong polarized intensities (more than 0.4 mJy/beam) are found in between and parts of the northern optical arms IV N and I N (see Fig. 3) and also in central regions of the galaxy. It seems that the polarized emisson, as a whole, obeys a spiral pattern structure. Whether this structure mimics the optical arm structure or not can be seen in Fig. 3, where a sketch of optical arms (Sandage & Humphreys 1980) is superimposed on the polarized intensity map. The polarized emission is found partly in the optical arms and partly in between the arms. In the other words, there is no clear correlation between the optical arms and polarization arm-like structure. The vectors in Fig. 1 (and also 2) show the intrinsic orientation of the ordered magnetic field in the plane of the sky (PI $\sim B^2_{\mathrm{reg}\perp}$), as Faraday rotation is not significant at 3.6 cm. A comparison between the orientation of the ordered magnetic field and optical structure is shown in Fig. 4. Again, it is seen that the ordered magnetic field traces out some sort of spiral structure that does not coincide closely with the optical spiral arms, although there is a general similarity in the orientations. The strongest arm-like filament of the magnetic field exists in between the northern optical arms IV N and V N, but also covers parts of these two arms. Generally, in some regions the ordered magnetic field aligns parts of the optical arms (like parts of the arms I N and V N), is driven to the optical interarms, or locally distorted in orientation. The last is mostly seen in the southern part of the galaxy.

The vector lengths in Fig. 2 represent the degree of polarization, P. Apart from the northern arm IV N, P is high not only where the polarized intensity is strong: the southern optical arms I S and II S also show high P (greater than 20%). The highest degree of polarization, ~40%, is found near NGC 604 at RA = $01^{\mathrm{h}}34^{\mathrm{m}}49.67^{\mathrm{s}}$ and Dec = +30°47′19.49″ (Fig. 3). However, it is less than 5% within the giant HII regions (e.g. NGC 604 and NGC 595). This, along with a weaker ordered magnetic field (and low P) in the central southern arm (I S, the strongest arm in radio, IR, and optical bands), indicates that high star-forming activity locally disturbs the regular magnetic field and causes the patchy distribution of the degree of polarization within the arms.

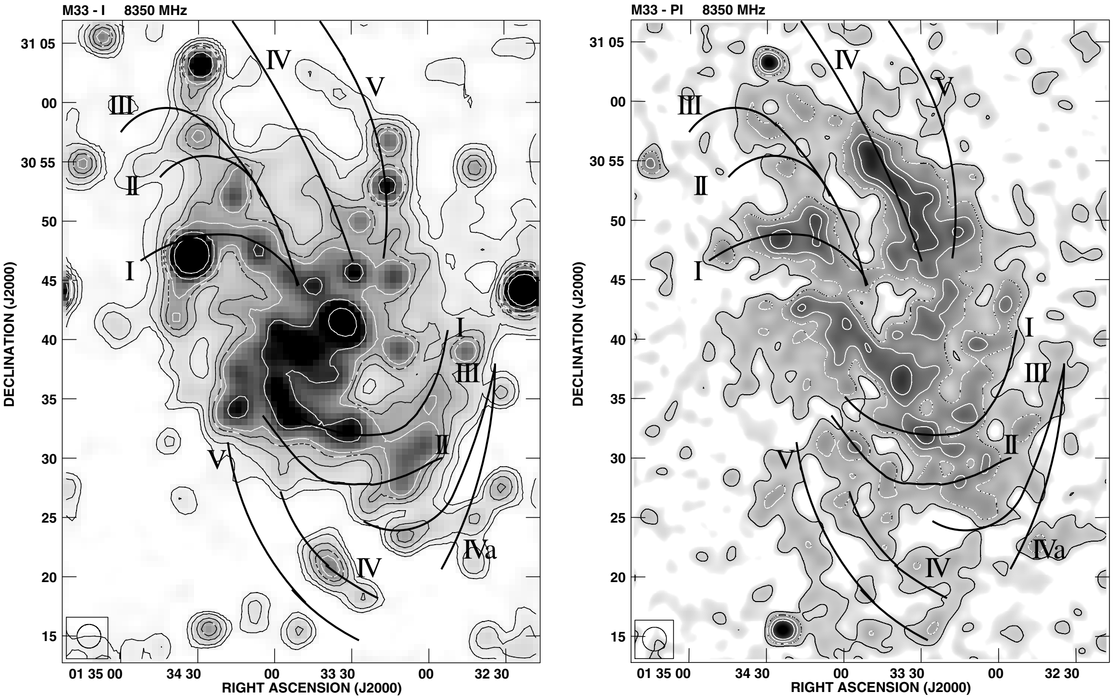

Fig. 3. A sketch of the optical arms (Sandage & Humphreys 1980) overlayed on the total (*left panel*) and linearly polarized (*right panel*) intensities at 3.6 cm. Grey scales and contour levels are the same as in Figs. 1 and 2.

Table 2. Characteristics and performances of the receivers of the 100-m Effelsberg telescope.

λ (cm)	3.6	6.2
Center frequency (GHz)	8.350	4.850
Band width (MHz)	1100	500
HPBW (″)	83.6	146
$T_{\rm sys}$ (K)	23–25	25–28
$T_{\rm b}/S_{\nu}$ (K/Jy)	2.62	2.4

At the angular resolution of 180″ at 6.2 cm, the magnetic arm-like filaments are smoother and not very distinguishable (Fig. 6). The strong polarized emission (more than 1.2 mJy/beam) again occurs in parts of the arms IV N and I N, but in contrast to the 3.6 cm polarized emission, not in the central regions of the galaxy (Fig. 5). The high P at 6.2 cm (>20%) has almost the same distribution as at 3.6 cm. In the arm IV N, the maximum P is about 30%, similar to that at 3.6 cm.

Figure 7 shows, at a linear resolution of ~200 pc, how the apparent magnetic field vectors (E+90°) at 20 cm are distributed in the plane of the sky. At this wavelength, the vectors are strongly Faraday-rotated and therefore not oriented along the optical arms. The polarized signal is strongest in the northern part of the galaxy, where the ordering in a spiral-like pattern is very clear (Fig. 8), while the lack of polarized emission in the southern part suggests stronger Faraday depolarization in the southern than in the northern part of M 33 (see Sect. 3.6). In the northern arms, the degree of polarization P is greater than 20%, with a maximum of 30% on the arm IV N and also in a region close to NGC 604 in I N.

3.3. Integrated flux densities

After subtraction of the background sources (14 sources whose 20 cm flux densities were ≥5 mJy/beam), we integrated the flux densities in rings in the plane of the galaxy around the center out to a radius of 8.5 kpc (beyond the area shown in Figs. 1 to 8, see Table 1). The integrated flux density in total intensity, $S_{\rm T}$, and in linear polarization, $S_{\rm PI}$, at different wavelengths are given in Table 5. The corresponding absolute total flux density errors were obtained considering the systematic error due to the baselevel uncertainty.

The average degree of polarization ($\bar{P}$), which is the ratio of the integrated flux density in polarized intensity and the integrated flux density in total intensity, is obtained at different wavelengths (Table 5). For a consistent comparison, we also obtained the average degree of polarization after smoothing the 3.6 cm and 20 cm maps to the beam width of 180″, $\bar{P}(180'')$. At 3.6 cm and 20 cm, $\bar{P}(180'')$ is lower than $\bar{P}$ due to beam depolarization, while $\bar{P}(180'')$ is almost the same at 3.6 cm and 6.2 cm, indicating negligible global Faraday depolarization between these two wavelengths.

The integrated total flux densities in total intensity obtained by Buczilowski (1988) of 1100 ± 167 mJy at 6.3 cm and 2990 ± 440 mJy at 20 cm out to a radius of 12 kpc agree with our values of 1300 ± 140 mJy at 6.3 cm and 3164 ± 88 mJy at 20 cm within the errors. Our obtained value at 6.2 cm is even closer to the one obtained by Berkhuijsen (1983) (1300 ± 200 mJy). The integrated total flux density in total intensity found by Buczilowski (1988) at 2.8 cm is significantly lower than what we found at 3.6 cm because the galaxy size is much larger than the maximum spacing of the 2.8 cm multibeam system (Emerson et al. 1979).

3.4. Distribution of total spectral index

Because of their wide frequency range, the total intensities at 20 cm and 3.6 cm lead to a reliable spectral index map. After smoothing to the angular resolution of 90″, the total intensity maps at 20 cm and 3.6 cm were restricted to a common size and interpolated onto the same grid. The spectral index, α ($I \sim \nu^{-\alpha}$),

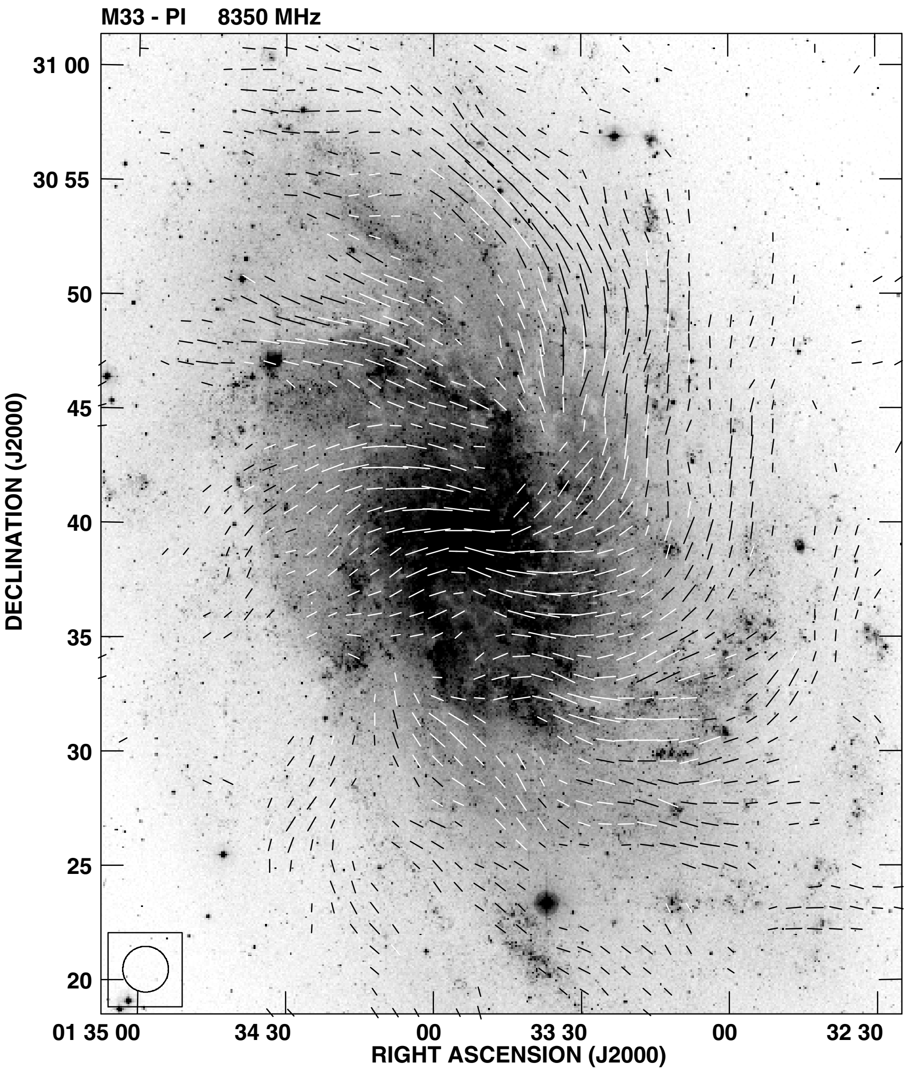

Fig. 4. Apparent ***B***-vectors (***E***-vectors rotated by 90°) at 3.6 cm superimposed on an optical image (*B*-band, taken from the STScI Digitized Sky Survey) of M 33. A vector length of 1′ represents a polarized intensity of 0.3 mJy/beam. The vectors were plotted starting from 1.5σ.

Table 3. Central positions of the 12 fields observed with VLA at 20 cm.

Pointing #	RA (α) ($^{\mathrm{h\ m\ s}}$)	Dec (δ) ($^{\circ}\ '\ ''$)	*I* rms noise (μJy/beam)	*U* (*Q*) rms noise (μJy/beam)	*HPBW* (arcsec^2)
1	01 35 01.26	+30 16 45.00	26	23	50.7 × 49.5
2	01 33 51.79	+30 16 45.00	23	20	50.2 × 46.1
3	01 32 42.31	+30 16 45.00	27	18	50.6 × 43.4
4	01 35 01.26	+30 31 45.00	26	21	48.1 × 44.0
5	01 33 51.60	+30 31 45.00	28	20	47.8 × 45.4
6	01 32 41.96	+30 31 45.00	32	19	51.4 × 42.2
7	01 35 01.26	+30 46 45.00	26	21	50.0 × 46.1
8	01 33 51.41	+30 46 45.00	34	21	49.2 × 42.4
9	01 32 41.58	+30 46 45.00	23	19	51.1 × 44.0
10	01 35 01.26	+31 01 45.00	36	23	48.5 × 45.2
11	01 33 51.21	+31 01 45.00	24	21	51.1 × 43.3
12	01 32 41.21	+31 01 45.00	21	19	48.0 × 44.0

was only computed for pixels with a flux density of at least three times the rms noise σ at both frequencies. In the resulting spectral index map (Fig. 9), the spiral arms and star-forming regions are very visible as flat spectrum regions. Steeper spectra occur in the outer regions and in between arms. Figure 10 shows that the total spectral index has a mean value of 0.7. The error in the total spectral index varies from 0.01 in the star-forming regions to 0.23 in the outer parts.

The HII complexes IC 133, NGC 604, and NGC 595 have spectral indices <0.1 and even negative values, indicating optically thick conditions in these HII regions. Johnson et al. (2001) found several optically thick HII regions (at 6 cm and 20 cm) with the two brightest ones in IC 133.

The most inverted spectrum is due to a source at RA = $01^{\mathrm{h}}32^{\mathrm{m}}42.06 \pm 0.14^{\mathrm{s}}$ and Dec = $+30^{\circ}54'24.8 \pm 1.8''$, which has a spectral index of -0.6 ± 0.1 ($I_{3.6\ \mathrm{cm}} = 3.6 \pm 0.2$ and

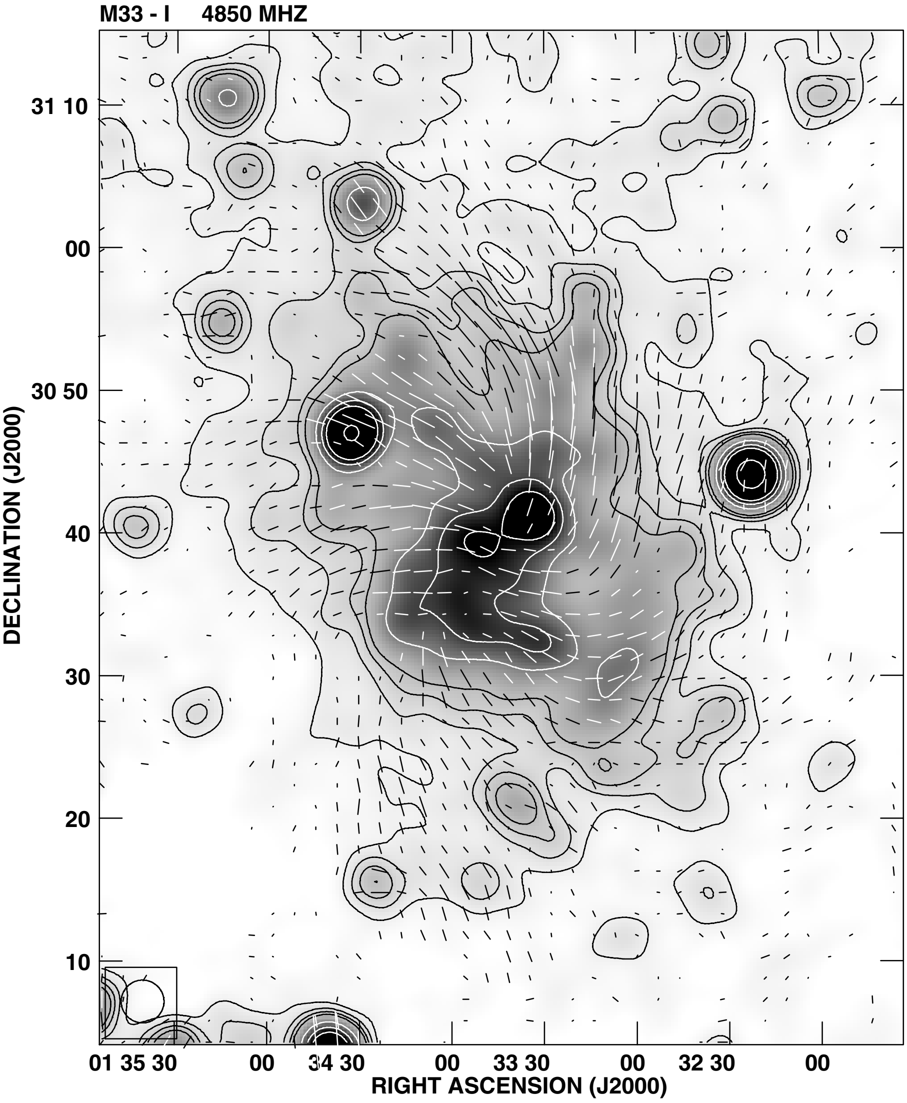

Fig. 5. Total intensity emission from M 33 at 6.2 cm observed with the Effelsberg telescope, with an angular resolution of 180″ (the beam area is shown in the left-hand corner). Apparent ***B***-vectors of the polarized intensity (***E***-vectors rotated by 90°) are superimposed. Contour levels are 2.2, 4.4, 6.6, 8.8, 17.6, 26.4, 35.2, 70.4 mJy/beam. The rms noise is 0.56 mJy/beam in total intensity and 0.12 mJy/beam in polarization. The vectors were plotted starting from 2.5σ. A vector length of 1.5′ represents a polarized intensity of 1 mJy/beam.

Table 4. The 11 brightest HII regions at 3.6 cm.

Object	RA (α) ($^{\rm h\ m\ s}$)	Dec (δ) ($^{\circ}\ '\ ''$)	Flux density (mJy/beam)
NGC 604	1 34 32.9	30 47 19.6	53.7 ± 0.4
NGC 595	1 33 32.4	30 41 50.0	20.7 ± 0.7
IC 133	1 33 15.3	30 53 19.7	9.4 ± 0.5
B690	1 34 06.5	30 47 40.0	5.3 ± 0.3
B61/62	1 33 44.8	30 44 50.0	4.9 ± 0.5
IC 132	1 33 17.1	30 56 51.8	4.7 ± 0.2
IC 131	1 33 12.5	30 45 21.5	4.7 ± 0.3
NGC 588	1 32 44.7	30 39 20.6	4.5 ± 0.3
IC 142	1 33 56.7	30 45 51.8	4.1 ± 0.2
B691	1 34 15.4	30 52 21.8	4.1 ± 0.5
NGC 592	1 33 12.6	30 38 51.3	4.1 ± 0.3

$I_{20\,\rm cm} = 1.24 \pm 0.07$). This source, which does not exist in the catalogues of radio sources and HII regions of M 33 (e.g. in Gordon et al. 1999), could be a variable radio source or a giant optically thick HII region behind a high concentration of dust. However, the latter possibility is unlikely, since no IR emission is observed from that region.

We obtained the radial distribution of the spectral index α using the integrated total flux densities calculated in rings with a width of 0.5 kpc in the galactic plane. Figure 11 presents the radial profile of the spectral index obtained from pairs of the integrated flux densities at 3.6 cm, 6.2 cm, and 20 cm considering one σ level. There is a general increase in α from the center to a radius of about 7 kpc in all three profiles. Buczilowski (1988) explained this increase as a general decrease in the thermal fraction with radius. However, with our high-resolution study, we detect structures not seen by Buczilowski (1988): a prominant bump around $R = 3$ kpc and a steeper increase in α beyond $R =$ 4 kpc. This indicates that the thermal fraction decreases faster in regions at $R > 4$ kpc than at smaller radii. The bump is located in the ring $2.5 < R < 3$ kpc dominated by interarm regions that are expected to be weak in thermal emission.

Assuming that the radial increase of the spectral index is related to a decrease in the thermal fraction, and considering that the thermal emission contributes more to the radio continuum emission at shorter wavelengths, one expects more variations (or faster radial increase) of the spectral index obtained at short wavelengths. This is indeed visible in Fig. 11: $\alpha(3.6, 6.2)$ increases faster than $\alpha(6.2, 20)$ and $\alpha(3.6, 20)$ at $R > 4$ kpc. It is also seen that the longer the wavelengths, the smaller the spectral index (or flatter energy spectrum at longer wavelengths). This is surprising because one expects that the spectrum of the radio continuum emission becomes steeper at longer wavelengths

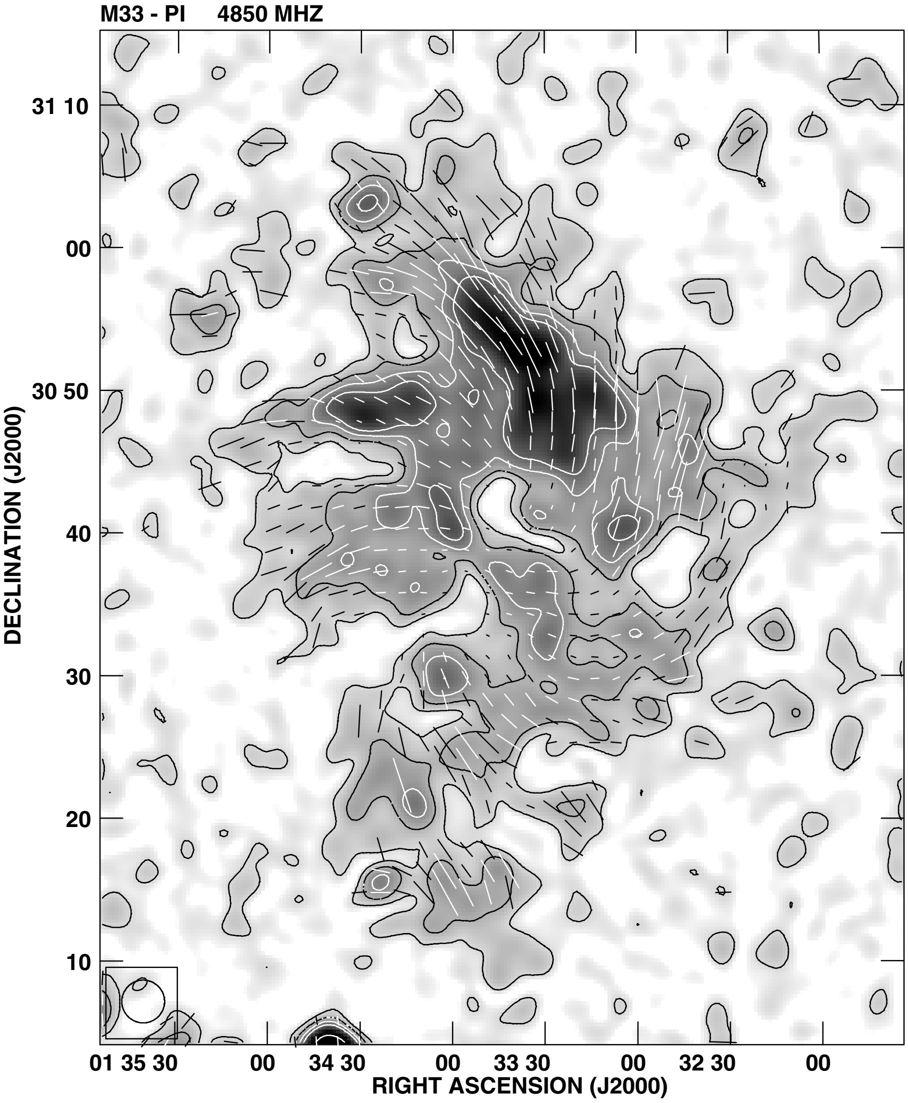

Fig. 6. Linearly polarized emission (contours and grey scale) and degree of polarization (vector lengths) from M 33 at 6.2 cm observed with the Effelsberg 100-m dish, with an angular resolution of 180″ (the beam area is shown in the left-hand corner). Position angles of the vectors show the orientaiton of the magnetic field component perpendicular to the line of sight. Contour levels are 0.3, 0.6, 0.9, 1.2, 2.4 mJy/beam area. The rms noise is 0.12 mJy/beam. A vector length of 1.5′ represents a degree of polarization of 11.7%.

due to the synchrotron emission. This could hint at the nonthermal energy losses at longer wavelengths. The reason may be the same as for the significant flattening of the integrated spectrum of M 33 at frequencies lower than 900 MHz: free-free absorption of the nonthermal emission by a cool (<1000 K) ionized gas (Israel et al. 1992). The presence of the optically thick HII regions (Johnson et al. 2001) could also enhance this trend.

Away from star-forming regions and in the outer parts of the galaxy, the thermal fraction is negligible and the observed spectral index α can be taken as the nonthermal spectral index, α_n. From Fig. 9, we obtain $\alpha_n \simeq 1.0 \pm 0.1$, which is equal to what is found in M 31 by Berkhuijsen et al. (2003). Assuming that the nonthermal spectral index is constant across M 33, we find average thermal fractions of 0.52 ± 0.15, 0.46 ± 0.12, and 0.18 ± 0.06 at 3.6 cm, 6.2 cm, and 20 cm, respectively (following the method by Klein et al. 1984). How these values change if the nonthermal spectral index is not assumed to be constant across the galaxy will be discussed in Paper II (Tabatabaei et al., in prep.).

3.5. Integrated radio continuum spectrum

The integrated flux densities for $R < 50'$ (12 kpc) from Effelsberg surveys at 35.6, 21.1, 17.4, 11.1, 6.3, and 2.8 cm were presented by Buczilowski (1988). They obtained a spectrum with a spectral index of 0.91 ± 0.13, steeper than found in many other spiral galaxies.

We rederived the integrated spectrum of M 33 using three more data points from the new surveys. We calculated the integrated flux densities for the 3.6, 6.2, and 20 cm maps for the same area of $R < 50'$. The 3.6 cm and 2.8 cm maps were integrated up to $R = 44'$ and $R = 22.5'$, respectively, providing a lower limit to the total flux density. However, extrapolated values up to $R = 50'$ show that the missing flux densities are within errors. Our values, together with those of Buczilowski (1988) (see Table 6), lead to an integrated spectrum (Fig. 11) with a spectral index of 0.72 ± 0.04, which agrees with the mean spectral index obtained in Sect. 3.4 even though using a different method.

3.6. Exponential scale lengths

Figure 13 shows the radial distributions of the total radio and IR (Spitzer 24, 70, and 160 μm) intensities in M 33 with galactocentric radius. There is a break in the profiles near $R = 4$ kpc, which can be seen best at 3.6 cm and 24 μm. All the profiles can be well-fitted by two exponential functions of the form

$$I(R) = \begin{cases} I_0 \exp\left(-R/l_{R<4\ \mathrm{kpc}}\right) & R < 4\ \mathrm{kpc} \\ I_4 \exp\left(-R/l_{R>4\ \mathrm{kpc}}\right) & R \geq 4\ \mathrm{kpc}, \end{cases} \tag{1}$$

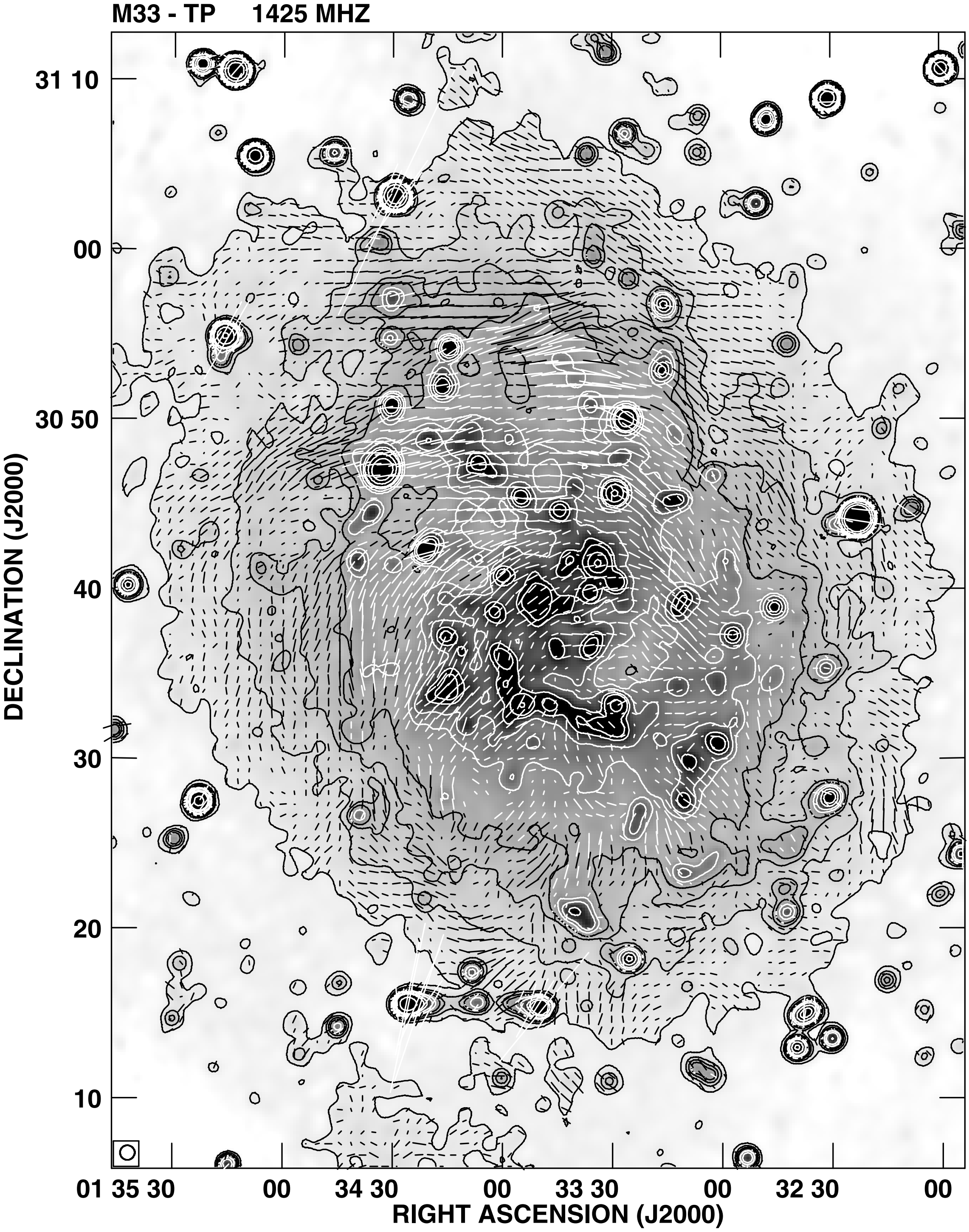

Fig. 7. The combined VLA + Effelsberg map of the total intensity emission from M 33 at 20 cm, with apparent ***B***-vectors of polarized intensity (***E***-vectors rotated by 90°) superimposed. The *HPBW* is 51″ (the beam area is shown in the left-hand corner). Contour levels are 0.3, 0.6, 0.9, 1.2, 1.8, 2.4, 3.6, 4.8, 9.6, 19.2 mJy/beam. The rms noise is 0.07 mJy/beam in total intensity and 0.025 mJy/beam in polarization. The vectors were plotted starting from 1.5σ. A vector length of 51″ represents a polarized intensity of 0.1 mJy/beam.

Table 5. Integrated flux densities for $R < 8.5$ kpc (35′).

λ (cm)	*HPBW* (arcsec^2)	$S_{\rm T}$ (mJy)	$S_{\rm PI}$ (mJy)	$\bar{P}$ %	$S_{\rm PI}(180'')$ (mJy)	$\bar{P}(180'')$ %
3.6	120	779 ± 66	48 ± 5	6.1 ± 0.8	40 ± 4	5.1 ± 0.7
6.2	180	1284 ± 135	89 ± 4	6.9 ± 0.8	89 ± 4	6.9 ± 0.8
20 (combined)	51	2768 ± 63	167 ± 25	6.0 ± 0.9	123 ± 3	4.4 ± 0.1

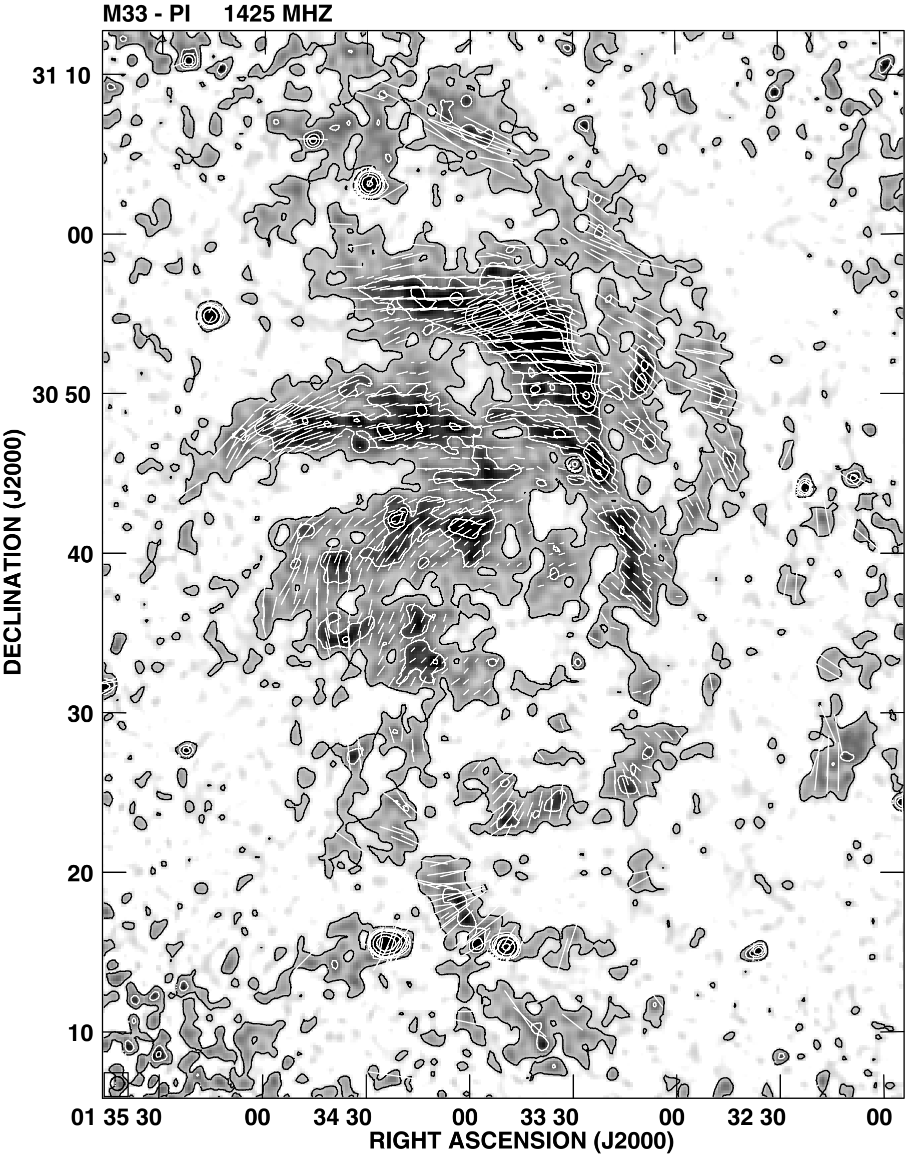

Fig. 8. The combined VLA + Effelsberg map of the linearly polarized emission (contours and grey scale) and degree of polarization (vector lengths) from M 33 at 20 cm. The *HPBW* is 51″ (the beam area is shown in the left-hand corner). Contour levels are 0.07, 0.14, 0.21, 0.28, 0.42, 0.56, 0.84 mJy/beam. The rms noise is 0.015 mJy/beam. A vector length of 51″ represents a degree of polarization of 8.7%.

Table 6. Integrated total flux densities from Effelsberg surveys ($R < 50'$).

λ (cm)	ν (MHz)	S (mJy)
35.6	842	5377 ± 1217[1]
21.1	1420	2990 ± 440[1]
20 (21)	1425	2768 ± 63[2]
17.4	1720	2714 ± 254[1]
11.1	2702	1683 ± 168[1]
6.3	4750	1100 ± 167[1]
6.2	4850	1300 ± 135[2]
3.6	8350	779 ± 66[2]
2.8	10 700	482 ± 150[1]

[1] Buczilowski (1988). [2] This paper.

Table 7. Exponential scale lengths.

λ	$l_{R<4\ \mathrm{kpc}}$ (kpc)	$l_{R>4\ \mathrm{kpc}}$ (kpc)
20 cm	5.44 ± 0.27	2.74 ± 0.10
6.2 cm	3.73 ± 0.21	2.35 ± 0.14
3.6 cm	3.48 ± 0.53	1.29 ± 0.03
24 μm	2.07 ± 0.23	1.35 ± 0.09
70 μm	2.04 ± 0.19	1.85 ± 0.16
160 μm	2.51 ± 0.19	1.63 ± 0.09

where, I_0 and I_4 are the intensity at $R = 0$ and $R = 4$ kpc, respectively, and l the exponential scale length.

We derived the exponential scale lengths of the radio emission at the three wavelengths along with those of the IR emission (Table 7). Generally, the scale lengths are larger in regions at $R <$ 4 kpc than at $R > 4$ kpc. This indicates that the surface brightness decreases faster with increasing radius at $R > 4$ kpc at all wavelengths. Since the 24 μm emission (and also 3.6 cm emission, Tabatabaei et al. 2007) traces the star-forming regions, this confirms that the main star-forming regions in M 33 are spread over an area with a radius of $R < 4$ kpc without a dominant "nuclear concentration" (different from the situation in NGC 6946, Walsh et al. 2002).

Table 7 also shows that the scale length increases with increasing wavelength in the radio regime. This can be explained by the fact that at longer wavelengths the nonthermal emission becomes more dominant, and the influence of radial diffusion of

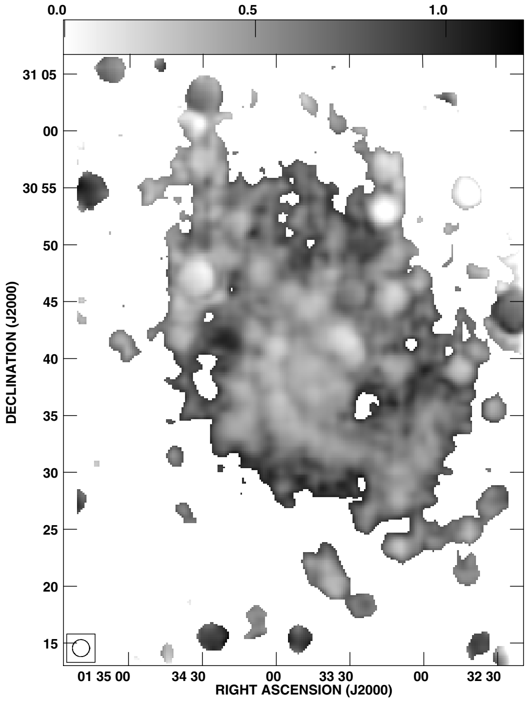

Fig. 9. Total spectral index map of M 33 as determined between the two wavelengths 3.6 and 20 cm. The angular resolution is 90″. For the total intensity maps, 3σ level was considered to obtain this spectral index map.

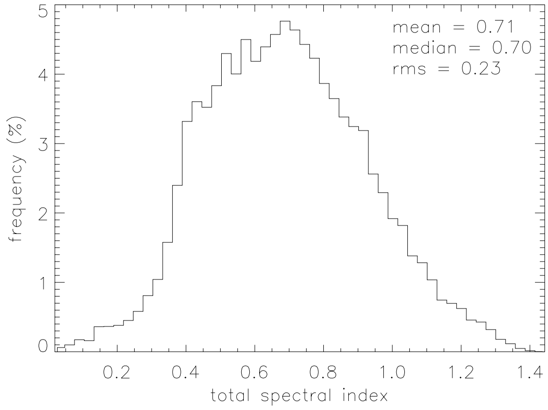

Fig. 10. Histogram of the spectral index distribution determined from total intensities.

cosmic ray electrons becomes more important, leading to larger scale lengths.

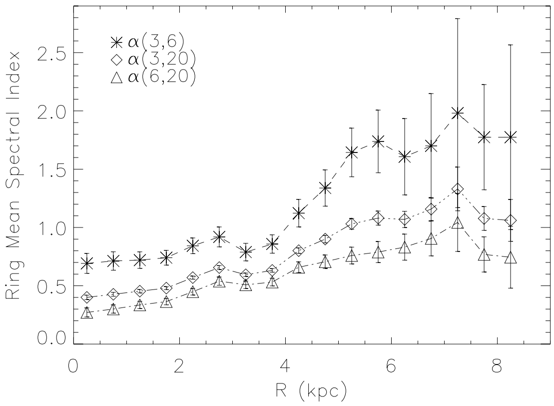

Fig. 11. Total spectral index averaged in rings of 0.5 kpc width in the galactic plane versus the radial distance from the center of M 33. For the total intensity maps, one σ level was considered before integration.

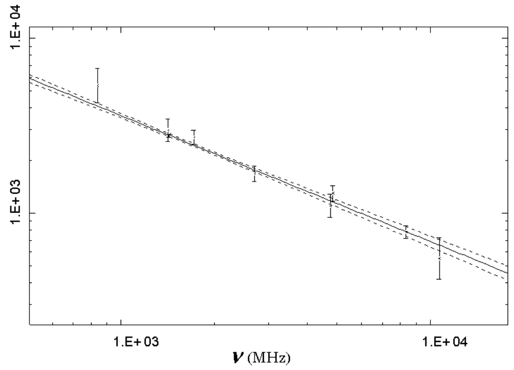

Fig. 12. Radio spectrum of the integrated emission from M 33 using the data listed in Table 6.

3.7. North-south asymmetry

Figure 7 shows that the polarized emission at 20 cm is much weaker in the southern than in the northern half. To investigate this asymmetry, we calculated the integrated total flux density in both total and polarized intensities separately over each half (Table 8). The average degrees of polarization are also given in Table 8. At all three radio wavelengths, the beam width is 180″. The ratio of the northern to the southern integrated total flux density in polarized intensity, $S^{\mathrm{N}}_{\mathrm{PI}}/S^{\mathrm{S}}_{\mathrm{PI}}$, and also the ratio of the average degree of polarization, $\bar{P}^{\mathrm{N}}/\,\bar{P}^{\mathrm{S}}$, increases with wavelength. The value of $S^{\mathrm{N}}_{\mathrm{T}}/S^{\mathrm{S}}_{\mathrm{T}}$ does not change from 3.6 cm to 6.2 cm and from 6.2 cm to 20 cm within the errors, but, it decreases slightly from 3.6 cm to 20 cm. A wavelength-dependent asymmetry in the polarized intensity and average degree of polarization was also found in other galaxies e.g. NGC 6946 (Beck, submitted to A&A). The interpretation is that there is an asymmetry in Faraday depolarization along the line of sight that may be caused in several ways:

- asymmetry in the distribution of the thermal emission;
- asymmetry in the uniformity of the magnetic field strength;
- special large-scale structure of the regular magnetic field, like e.g. a large-scale axisymmetric helical magnetic field (Urbanik et al. 1997).

We will investigate these possibilities after the separation of thermal/nonthermal components in a forthcoming paper (Tabatabaei et al., in prep.).

4. Discussion and conclusions

Radio observations with high resolution and sensitivity enabled us to obtain much more information about the distribution of the linearly polarized emission in M 33 than in previous studies, especially at high frequencies where the Faraday effects are negligible. Using the new data at 3.6 cm, we found that the magnetic field is well-ordered in a spiral structure with the general orientation of the optical spiral arms. No clear anti-correlation between the ordered magnetic field and optical arms, as observed in other galaxies like NGC 6946 (Beck & Hoernes 1996), M 81 (Krause et al. 1989a), and in parts of IC 342 (Krause et al. 1989b; Krause 1993), is found in M 33. Detection

Table 8. Northern and southern integrated flux densities in total and polarized intensity plus degree of polarization.

λ cm	$S_{\rm T}^{\rm N}$ (mJy)	$S_{\rm T}^{\rm S}$ (mJy)	$S_{\rm T}^{\rm N}/S_{\rm T}^{\rm S}$	$S_{\rm PI}^{\rm N}$ (mJy)	$S_{\rm PI}^{\rm S}$ (mJy)	$S_{\rm PI}^{\rm N}/S_{\rm PI}^{\rm S}$	$\bar{P}^{\rm N}$ %	$\bar{P}^{\rm S}$ %	$\bar{P}^{\rm N}/\bar{P}^{\rm S}$
3.6	412 ± 18	366 ± 21	1.12 ± 0.08	20 ± 2	20 ± 2	1.00 ± 0.14	4.8 ± 0.4	5.5 ± 0.6	0.9 ± 0.1
6.2	631 ± 63	653 ± 70	0.97 ± 0.14	53 ± 4	36 ± 2	1.47 ± 0.14	8.4 ± 1.0	5.5 ± 0.6	1.5 ± 0.2
20	1268 ± 73	1435 ± 83	0.88 ± 0.07	81 ± 5	42 ± 3	1.93 ± 0.18	6.4 ± 1.1	2.9 ± 0.3	2.2 ± 0.4

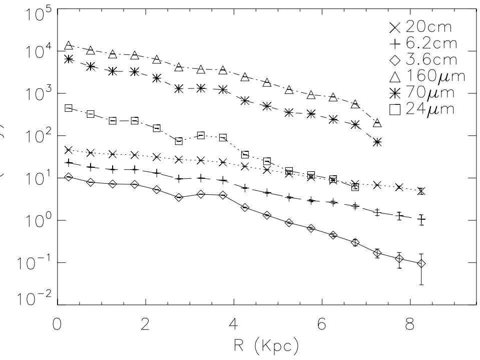

Fig. 13. Radial profiles of total intensity (surface brightness) at radio and IR wavelengths.

of high degrees of polarization (higher than 20%), not only in the northern arms but also in the central extended region and in parts of the southern arms at 3.6 cm and 6.2 cm (for the first time), is another significant result of this study. Generally, we found a patchy distribution of the degree of polarization. The degree of polarization in the direction of the HII complexes is less than 5%. We also found a weak degree of polarization and some distortion in the regular magnetic field in the central I S, which could be linked to the high star-forming activity in this region.

We derived a spectral index map of M 33 with a high angular resolution (90″) (the previous spectral index map was derived at 462″, Buczilowski 1988). Both the mean total spectral index (0.72 ± 0.07, obtained from the 3.6 and 20 cm maps) and the total spectral index obtained from the integrated spectrum (0.72 ± 0.04) are consistent with the result of a statistical study of 56 spiral galaxies by Gioia et al. (1982).

The radial profile of the spectral index (Fig. 11) shows not only a general increase but also fluctuations at $2 < R < 4$ kpc, confirming that the decrease in the thermal fraction causes an increase in the spectral index. Considering Fig. 13, at $2 < R < 4$ kpc, we found opposite fluctuations in total intensity and in spectral index. These fluctuations (in Fig. 13) are again stronger at wavelengths at which either the thermal emission is stronger (i.e. 3.6 cm) or the emission correlates well with the thermal emission (i.e. 24 μm, see Tabatabaei et al. 2007). The area at $2 < R < 3$ kpc includes the region between the main arm I (IN, IS) and the central extended region of the galaxy, corresponding to the small maximum (bump) in the spectral index profile and a small minimum in the total intensity profile. The area at $3 < R < 4$ kpc includes the arm I N and NGC 604, corresponding to the small minimum in Fig. 11 and the small maximum in Fig. 13.

Like the star formation radial profile (24 μm radial profile, see Sect. 3.6), the mostly nonthermal 20 cm radial profile is fitted by a larger exponential scale length at $R < 4$ kpc than at $R > 4$ kpc. This is a surprising result, indicating that even the nonthermal emission (which is less confined to the star-forming regions than the thermal emission) mimics the distribution of its parents, the star-forming regions. A spatial coupling between the nonthermal emission and star-forming regions was also found in other late-type galaxies (Dumke et al. 2000; Chyży et al. 2007). Therefore, it would be highly interesting to derive the distribution of the nonthermal emission for a more realistic non-constant spectral index of the nonthermal emission (Tabatabaei et al., Paper II).

Acknowledgements. We are grateful to E. M. Berkhuijsen and R. Wielebinski for valuable and stimulating comments. We thank the staff of 100-m Effelsberg telescope and VLA for their assistance with radio observations. F. Tabatabaei was supported for this research through a stipend from the International Max Planck Research school (IMPRS) for Radio and Infrared Astronomy at the Universities of Bonn and Cologne.

References

Baars, J. W. M., Genzel, R., Pauliny-Toth, I. I. K., & Witzel, A. 1977, A&A, 61, 99
Beck, R. 1979, Ph.D. Thesis, Rheinische Friedrich-Wilhelms-Universitaet, Bonn
Beck, R., & Hoernes, P. 1996, Nature, 379, 47
Berkhuijsen, E. M. 1983, A&A, 127, 395
Berkhuijsen, E. M., Beck, R., & Hoernes, P. 2003, A&A, 398, 937
Buczilowski, U. R. 1988, A&A, 205, 29
Buczilowski, U. R., & Beck, R. 1987, A&AS, 68, 171
Buczilowski , U. R., & Beck , R. 1991, A&A, 241, 47
Chyży, K. T., Bomans, D. J., Krause, M., et al. 2007, A&A, 462, 933
de Vaucouleurs, G., & Leach, R. W. 1981, PASP, 93, 190
Deul, E. R., & van der Hulst, J. M. 1987, A&AS, 67, 509
Dumke, M., Krause, M., & Wielebinski, R. 2000, A&A, 355, 512
Duric, N., Viallefond, F., Goss, W. M., & van der Hulst, J. M. 1993, A&AS, 99, 217
Emerson, D. T., & Graeve, R. 1988, A&A, 190, 353
Emerson, D. T., Klein, U., & Haslam, C. G. T. 1979, A&A, 76, 92
Fletcher, A. 2001, Ph.D. Thesis, University of Newcastle, UK
Freedman , W. L., Wilson , C. D., & Madore , B. F. 1991, ApJ, 372, 455
Gioia, I. M., Gregorini, L., & Klein, U. 1982, A&A, 116, 164
Gordon, S. M., Duric, N., Kirshner, R. P., Goss, W. M., & Viallefond, F. 1999, ApJS, 120, 247
Haslam, C. G. T. 1974, A&AS, 15, 333
Humphreys, R. M., & Sandage, A. 1980, ApJS, 44, 319
Israel, F. P., & van der Kruit, P. C. 1974, A&A, 32, 363
Israel, F. P., Mahoney, M. J., & Howarth, N. 1992, A&A, 261, 47
Johnson, K. E., Kobulnicky, H. A., Massey, P., & Conti, P. S. 2001, ApJ, 559, 864
Killeen, N. E. B., Bicknell, G. V., & Ekers, R. D. 1986, ApJ, 302, 306
Klein, U., Wielebinski, R., & Beck, R. 1984, A&A, 135, 213
Krause, M. 1993, in The Cosmic Dynamo, ed. F. Krause, K. H. Radler, & G. Rudiger, IAU Symp., 157, 305
Krause, M., Beck, R., & Hummel, E. 1989a, A&A, 217, 17
Krause, M., Hummel, E., & Beck, R. 1989b, A&A, 217, 4
Regan , M. W., & Vogel , S. N. 1994, ApJ, 434, 536
Sandage, A., & Humphreys, R. M. 1980, ApJ, 236, L1
Sofue, Y., & Reich, W. 1979, A&AS, 38, 251
Tabatabaei, F. S., Beck, R., Krause, M., et al. 2007, A&A, 466, 509
Terzian, Y., & Pankonin, V. 1972, ApJ, 174, 293
Urbanik, M., Elstner, D., & Beck, R. 1997, A&A, 326, 465
Viallefond, F., Goss, W. M., van der Hulst, J. M., & Crane, P. C. 1986, A&AS, 64, 237
von Kap-Herr, A., Berkhuijsen, E. M., & Wielebinski, R. 1978, A&A, 62, 51
Walsh, W., Beck, R., Thuma, G., et al. 2002, A&A, 388, 7